Electronic Supporting Information

Photocatalytic degradation of organic pollutants through conjugated poly(azomethine) networks based on terthiophene-naphthalimide assemblies

Matías J. Alonso-Navarro,[a,b] Jesús Barrio,[c,d] Sergio Royuela,[a,b] Neeta Karjule,[c] María M. Ramos,[b] José Ignacio Martínez,*[e] Menny Shalom,[c]* José L. Segura[a]*

a. Department of Organic Chemistry, Complutense University of Madrid, Faculty of Chemistry, Madrid 28040, Spain. E-mail: segura@ucm.es

b. Chemical and Environmental Technology Department. Univ. Rey Juan Carlos, Móstoles, 28933, Spain.

c. Department of Chemistry and Ilse Katz Institute for Nanoscale Science and Technology, Ben-Gurion University of the Negev, Beer-Sheva 8410501, Israel.

d. Department of Materials, Imperial College London, Royal School of Mines, London SW72AZ, England. E-mail: mennysh@bgu.ac.il

e. Department of Nanostructures and Low-dimensional Materials, Institute of Materials Science of Madrid (ICMM-CSIC), 28049 Madrid, Spain.

General Methods

Thin layer chromatography (TLC) was performed using pre-coated silica gel 60 F254 and compounds were visualized under UV light (λ = 254 nm). Solution ^{1}H-NMR and ^{13}C-NMR spectra were recorded on a Bruker AVIII-300 MHz spectrometer. Chemical shifts were reported in ppm and referenced to the residual non-deuterated solvent frequencies (CDCl$_3$: δ 7.26 ppm for ^{1}H, 77.16 ppm for ^{13}C). Mass spectra were recorded by means of matrix-assisted laser desorption/ionization time-of-flight (MALDI-TOF) or fast atom bombardment (FAB) ionization techniques.

Materials

1,3,5-tris-(4-aminophenyl)benzene (**TAPB**) and 5,5'-(2-(2-ethylhexyl)-1,3-dioxo-2,3-dihydro-1H-thieno[3'',4'':5',6']pyrazino[2',3':2,3]indeno[6,7,1-def]isoquinoline-7,9-diyl)bis(thiophene-2-carbaldehyde) (**NIP3T-2CHO**) were prepared according to previously reported procedures.[1, 2]

-NIP3T-ANW exfoliated material: 2 mg of **NIP3T-ANW** powder was sonicated in 4 mL of tetrahydrofuran for 1.5h in an Elmasonic P ultrasonic bath. The resulting colloidal dispersions were centrifuged at 1000 rpm for 5 min to eliminate non-exfoliated material, as it is described in the literature.[3]

Instrumental

- Fourier-transform infrared spectroscopy (FTIR). Solids were analysed by FTIR on a Bruker TENSOR 27 on a diamond plate (ATR).

- Powder X-ray diffraction (PXRD). PXRD measurements were carried out with X'PERT MPD with conventional Bragg-Brentano geometry using monochromatic Cu Kα1 radiation (λ = 1.5406 Å) in the 2θ = 2°-40° range.

 - Solid state ^{13}C cross-polarization magic angle spinning NMR (^{13}C-CP/MAS-NMR). ^{13}C-CP/MAS NMR spectra were recorded on a Bruker AVANCE III HD-WB 400 MHz with a rotation frequency of 12 kHz.

- N$_2$ sorption isotherms. N$_2$ (77 K) adsorption-desorption measurements were carried out on a Micromeritics Tristar 3000. Samples were previously activated for 4 h under high vacuum (<10^{-7} bar) at 120 ºC.

 - Thermogravimetric analysis (TGA). TGA was performed on a TGA-Q50 instrument on a platinum plate, heating the samples under nitrogen atmosphere at a heating rate of 10 °C/min.

- Dynamic light scattering (DLS). DLS studies were carried out using a Vasco 1 particle size analyser of Cordouan Technologies.

- Transmission electron microscopy (TEM). TEM micrographs and the corresponding selected area electron diffraction (SAED) patterns were recorded in a JEOL JEM 2100 TEM at 200 kV.

- The electrochemical properties of **NIP3T** and **NIP3T-ANW** were studied by cyclic voltammetry (Fig. 3) with a 0.1 M tetrabutylammonium hexafluorophosphate (TBAPF$_6$) solution in CH$_3$CN with scan rate of 50 mV s^{-1} in a three-electrode cell with Pt-foil as a counter electrode and Ag/AgCl (saturated KCl) reference electrode. The potential values were calibrated vs. Fc/Fc$^+$.

- The photocatalytic activity of the **NIP3T-ANW** was evaluated through the degradation of rhodamine B (**RhB**) in aqueous solution under visible light irradiation. In a typical **RhB**

degradation experiment, **NIP3T-ANW** sample (20 mg) and **RhB** solution (20 mL, 10 mg mL^{-1}) are mixed in a glass vial and exposed to sonication in a water bath to allow the dispersion of **NIP3T-ANW**. The vial is then kept in the dark under continuous stirring (800 rpm) until the adsorption-desorption equilibrium in reached. The reaction starts by irradiation with a white 50 W LED (Bridge lux BXRA-50C5300; λ>400 nm) and aliquots are withdrawn after certain time intervals. The **RhB** concentration was monitored spectrophotometrically utilizing its absorption maximum (λ = 554 nm) and plotted as normalized concentration C/C$_0$.

**Theoretical Methods and Computational Details**

Molecular fragments. First, molecular fragments of the 2D polymer under study were computed within the framework of the density functional theory (DFT) using the Gaussian16 program.[4] It is well-known that calculation of molecular fragments provide important information about the molecular, electronic structure and charge-transport properties of the formed 2D conjugated polymers.[5-7] To this end, two different hybrid functionals were used, such as the hybrid generalized gradient approximation (GGA) functional PBE0[8] and the long-range corrected hybrid functional CAM-B3LYP[9] together with the 6-31G**[10,11] and the cc-pVDZ[12] basis sets. All geometrical parameters were allowed to vary independently, and the calculated geometries were confirmed as minima by frequency calculations. Interestingly, PBE0 and CAM-B3LYP functionals and the two different 6-31G** and cc-pVDZ basis sets predict an almost identical description of their structural properties and topologies.

Periodic calculations. In a step forward, we used periodic boundary conditions to perform geometry optimization of a battery of stacked 3D layered models based on the canonical 2D network structure. For that purpose, the preliminary optimized building blocks can be considered as reasonable starting point geometries towards the assembling of the whole 2D network. Once the different models of the periodic system were constructed, they were fully optimized (simultaneous lattice/cell and structure optimizations) with the QUANTUM EXPRESSO plane-wave DFT code.[13] Within this implementation, the GGA-PBE[14] functional was used to account for the exchange-correlation (XC) effects, at the same time that we use the Grimme DFT-D3 semi-empirical efficient vdW correction to include dispersion forces and energies in conventional DFT functionals.[15] Ultra-soft pseudopotentials have been used to model the ion-electron interaction within the H, C, N, O and S atoms.[16,17] The Brillouin zones have been sampled by means of optimal Monkhorst-Pack grids.[18] One-electron wave-functions are expanded in a basis of plane-waves with a kinetic energy cutoff of 41 Ry for the kinetic energy and 260 Ry for electronic density. The energy cutoff values have been tested to achieve sufficient accuracy to guarantee a full convergence in total energy and electronic density. As mentioned, we have performed simultaneous full lattice/cell and structure optimizations for the different canonical layered 3D system models. The atomic relaxations were carried out within a conjugate gradient minimization scheme until the maximum force acting on any atom was below 0.02 eV Å^{-1}. Inter-layer distances have been fully-relaxed following the aforementioned simultaneous lattice/structure relaxation protocol. Different crystal-bulk models have been analyzed with several intermediate stacking-fashions between their both eclipsed (AA) and staggered (AB) configurations, which are hindered by steric impediment.

Topologies of valence and conduction bands. 3D isosurfaces of the orbital electronic densities corresponding to the valence and conduction electronic states of the different extended 2D COF systems studied here ($||\Psi_{cond}(\mathbf{r})||^2$ and $||\Psi_{val}(\mathbf{r})||^2$) have been plotted using the VMD 1.9.3 program (isosurface value of 0.0003 e$^-$/Å).[19] From these figures we can extract information about the spatial localization and delocalization degree of these states, which may directly connect

with the transport and optical performance of the systems, the homogeneity in the spatial distribution of the states, as well as their orbital character to permit dipolar transitions between them.[7]

UV-Vis spectra. Photoexcitation (optical absorption) spectrum of the most favorable periodic system (see Fig. S2) has been computed by the time-dependent DFT (TDDFT) formalism as implemented in the QUANTUM ESPRESSO simulation package.[20,21] Within this theoretical framework the excitation spectrum is obtained as $I(\omega) \propto Im[\bar{\alpha}(\omega)]$ (where $I(\omega)$ is the absorption intensity, and $Im[\bar{\alpha}(\omega)]$ is the imaginary part of $\bar{\alpha}(\omega)$, the averaged (average of the diagonal elements) dipole polarizability. This dynamical polarizability is represented in terms of the resolvent of its Liouvillian super-operator within TDDFT, and evaluated using a non-Hermitean Lanczos method, whose implementation does not require the calculation of virtual states.[20,21]
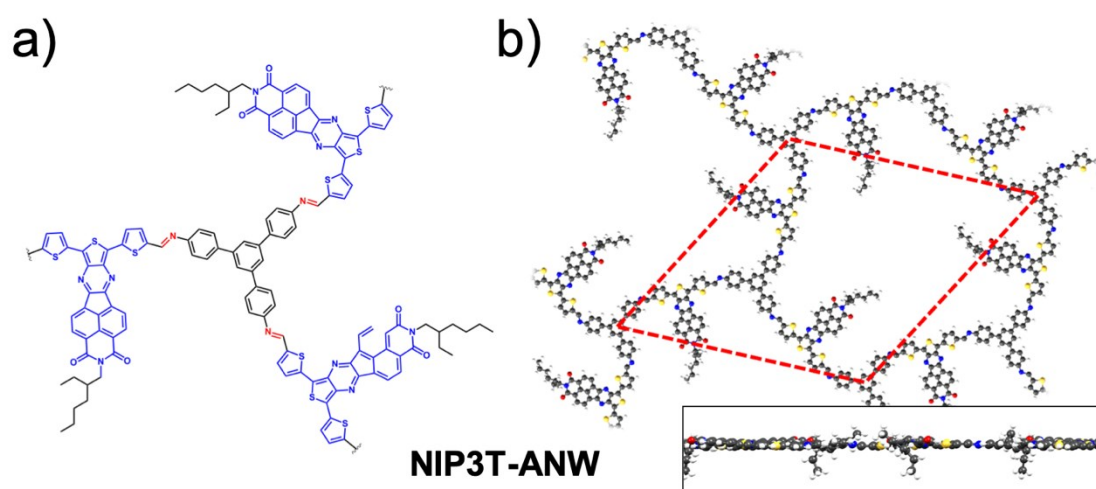
Figure S1. a) Chemical sketch of the formed **NIP3T-ANW** network. b) Pictorial top and side views of the fully optimized **NIP3T-ANW** 2D layer. White, grey, blue, red and yellow spheres correspond to H, C, N, O and S atoms, respectively. Dashed-red lined box represents the unit cell used in the calculations.
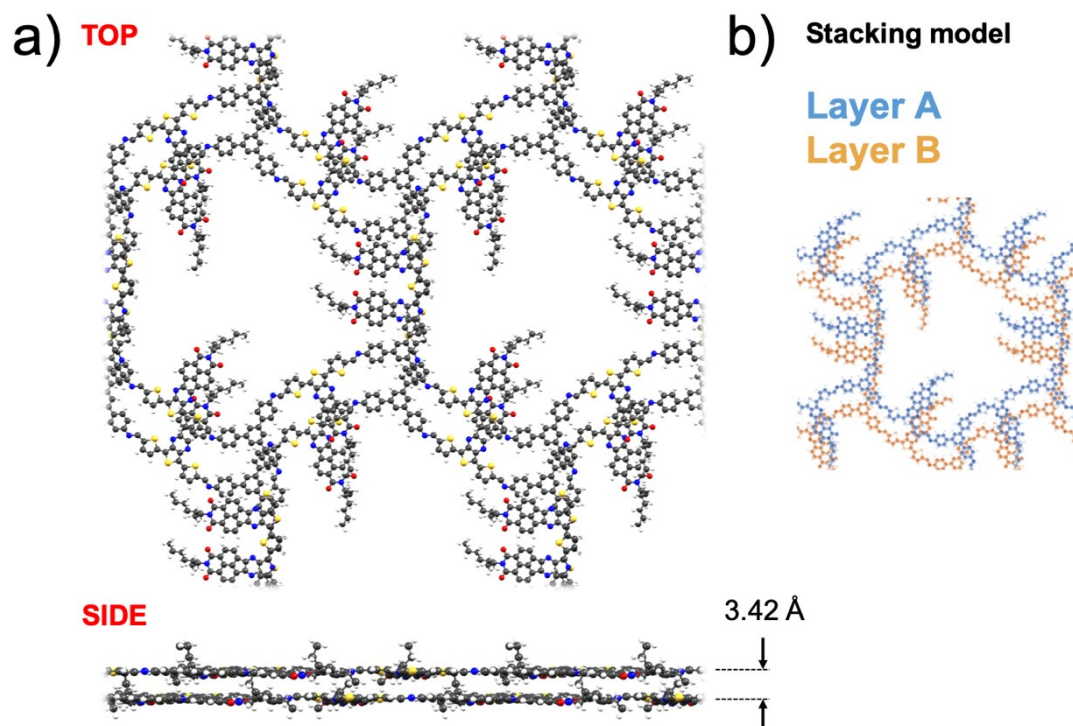
Figure S2. a) Pictorial top and side views of two fully optimized adjacent stacked layers for the most favorable computed **NIP3T-ANW** 3D crystal model. White, grey, blue, red and yellow spheres correspond to H, C, N, O and S atoms, respectively. Interlayer distance for the stacking in also indicated. b) Pictorial sketch of the most favorable stacking fashion obtained for the **NIP3T-ANW** 3D crystal.
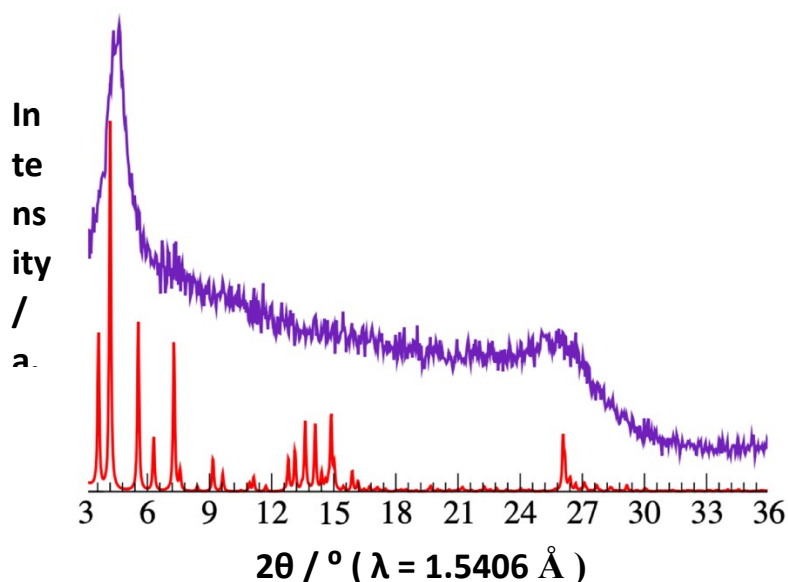
Figure S3. PXRD analysis of **NIP3T-ANW**: (purple line) experimental, and (red line) simulated on the basis of the most favourable 3D crystal arrangement.
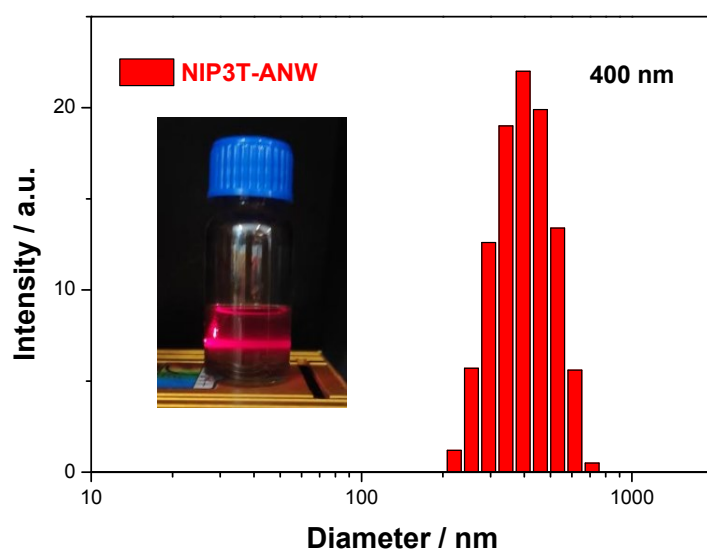
Figure S4. DLS measurement and Tyndall effect (inset) of exfoliated **NIP3T-ANW**.
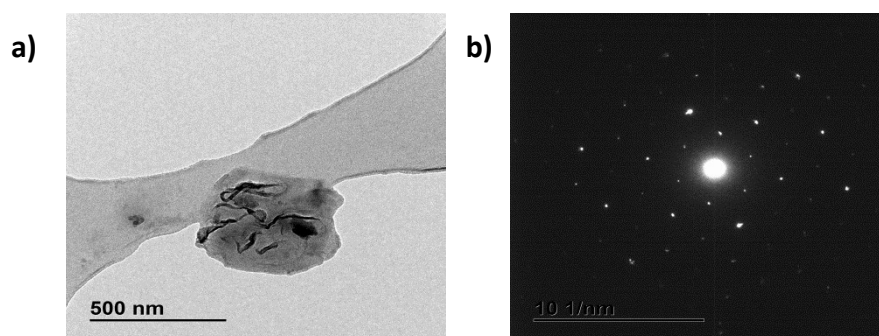

Figure S5. a) TEM images of **NIP3T-ANW** and b) SAED analysis of the sample.
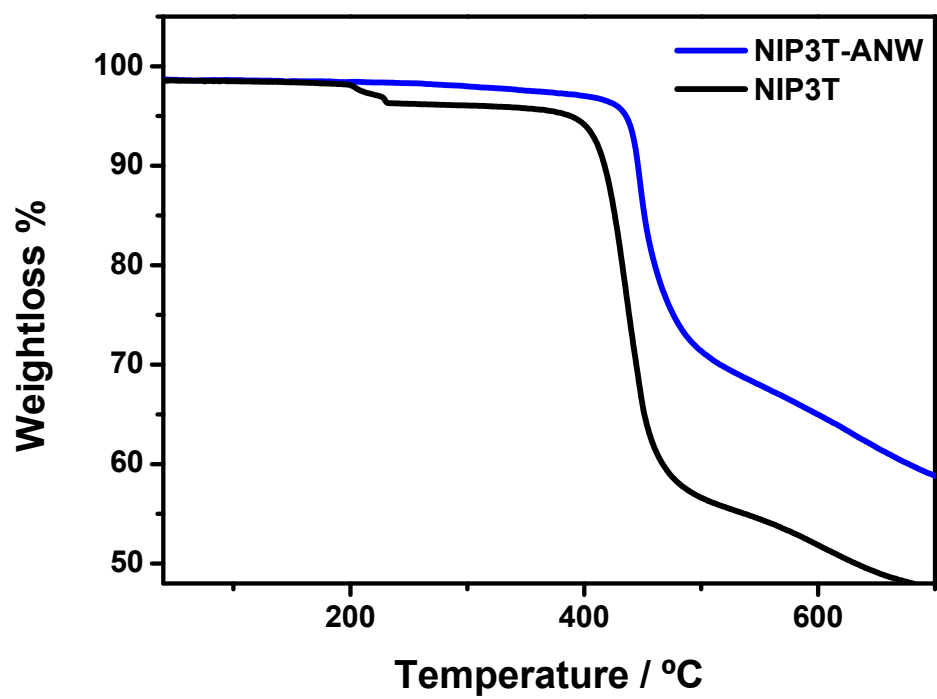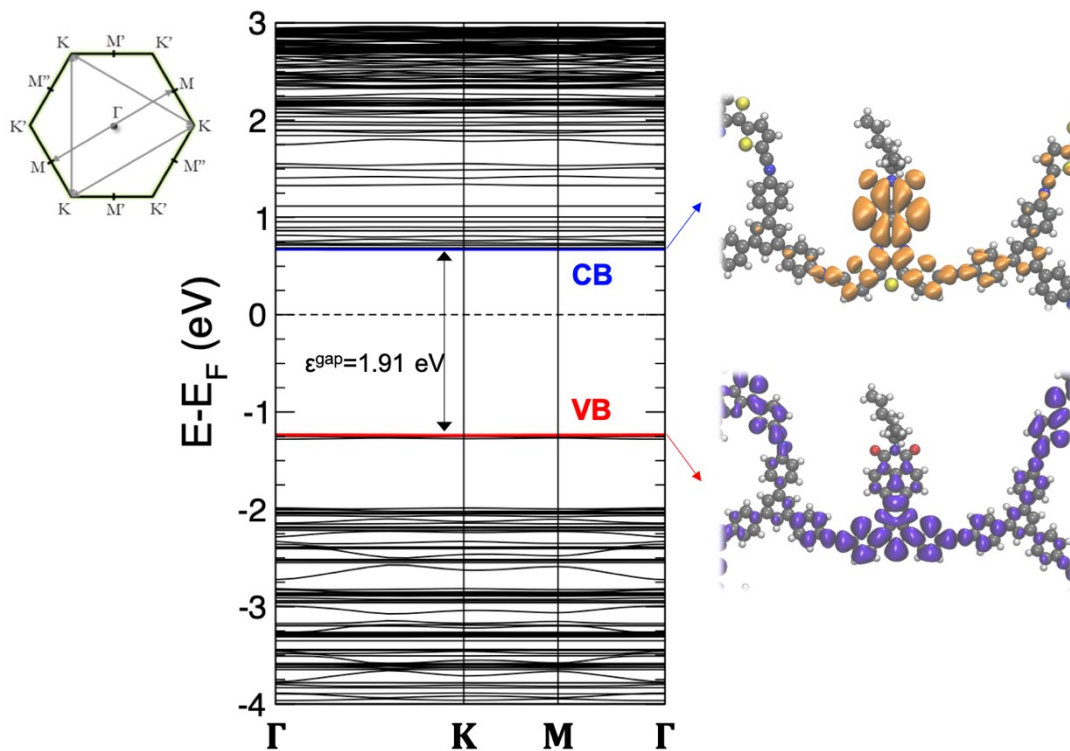
Figure S6. TGA curve of **NIP3T-ANW**.

Figure S7. Computed electronic band diagram of the most favorable crystal structure obtained along the high-symmetry k-path $\Gamma \rightarrow K \rightarrow M \rightarrow \Gamma$ (see inset), revealing a wide-gap (1.91 eV) semiconducting character of the compound. 3D orbital density isosurfaces corresponding to the valence and conduction bands (isosurface value of 0.0003 e$^-$/Å) are also shown in the figure.
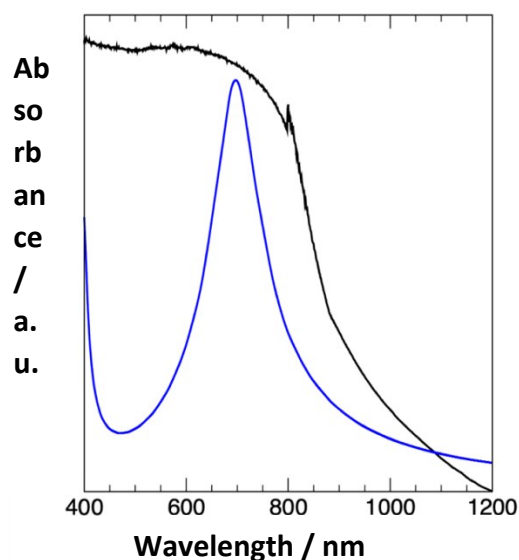
Figure S8. UV-vis Diffuse Reflectance for **NIP3T-ANW** as compared with the TDDFT photoabsorption spectra computed for the most favorable computed **NIP3T-ANW** 3D crystal model.
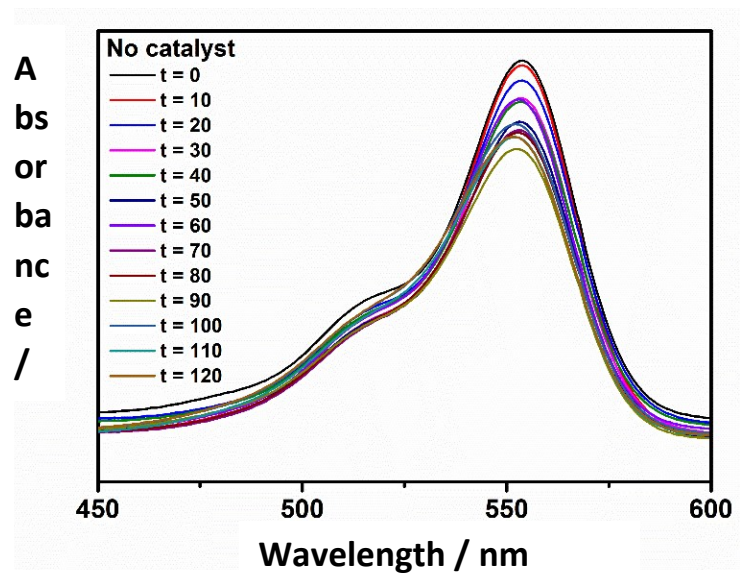
Figure S9. RhB degradation curves without catalyst.

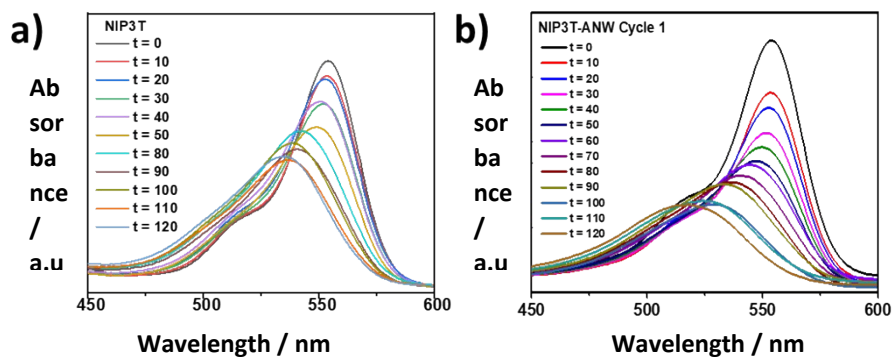**Figure S10. RhB** solutions after photocatalysis with **NIP3T** (left) and **NIP3T-ANW** after recycling test.

Figure S11. RhB degradation curves of a) **NIP3T** and b) **NIP3T-ANW**.
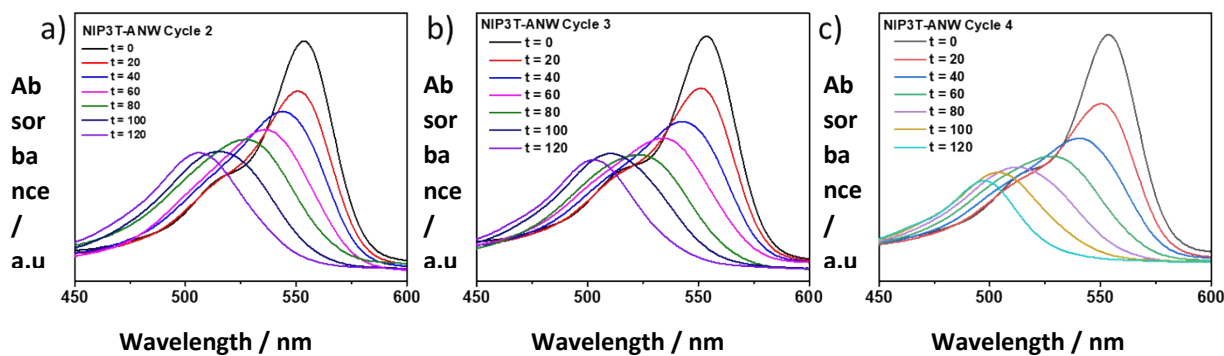

Figure S12. Cycles 2-4 (a-c) of **RhB** degradation curves utilizing **NIP3T-ANW** as photocatalyst.
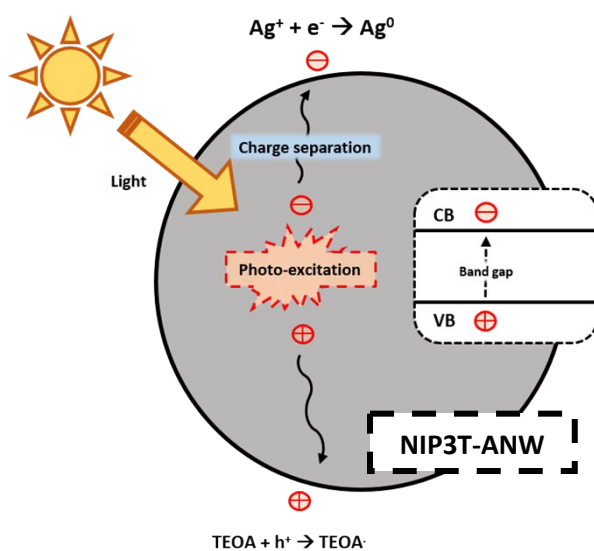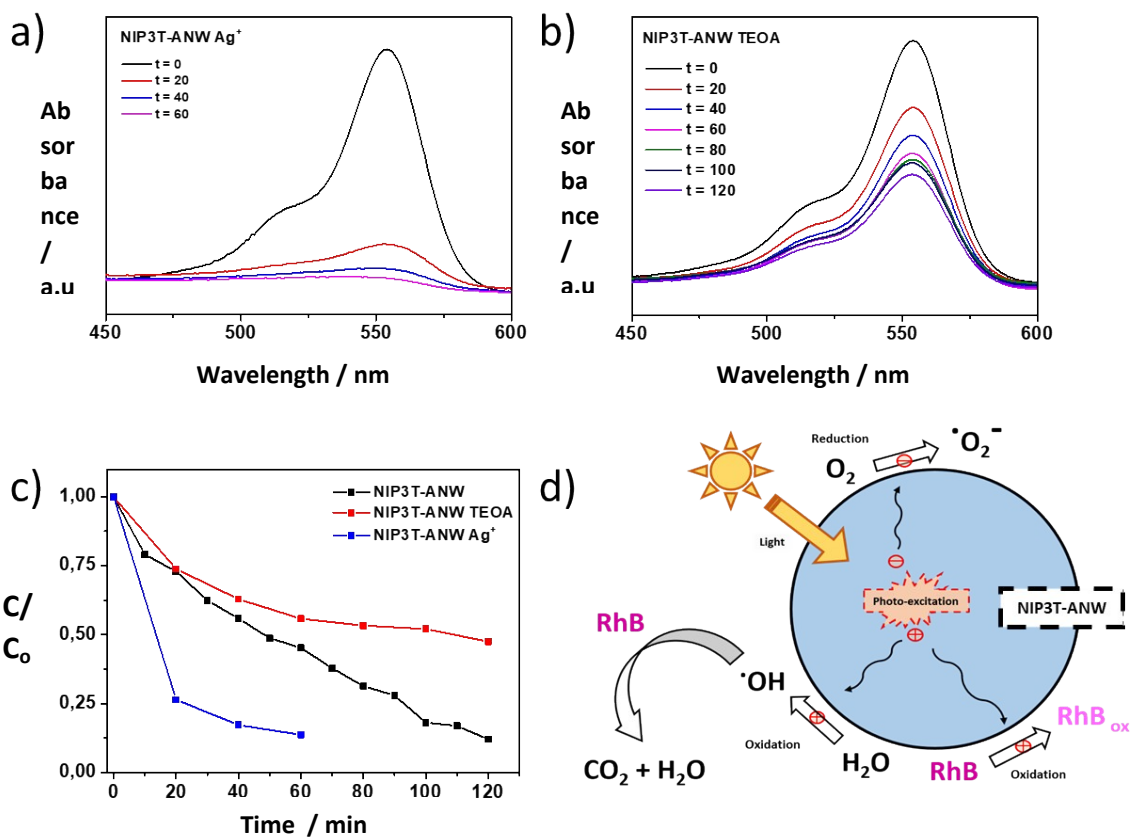

Figure S13. Schematic representation of the utilization of sacrificial agents for proving the **RhB** degradation mechanism.

Figure S14. RhB UV-vis degradation curves with **NIP3T-ANW** in the presence of Ag (a) and TEOA (b). Comparison of **RhB** degradation performances with different scavengers and in their absence (c). Schematic representation of the **RhB** degradation mechanism using **NIP3T-ANW** (d).

References

1. A. de la Peña Ruigómez, D. Rodríguez-San-Miguel, K. C. Stylianou, M. Cavallini, D. Gentili, F. Liscio, S. Milita, O. M. Roscioni , M. L. Ruiz-González, C. Carbonell, D. Maspoch, R. Mas-Ballesté, J. L. Segura and F. Zamora, *Chem. Eur. J.*, 2015, **21**, 10666-10670.

2. M. J. Alonso-Navarro, A. Harbuzaru, P. de Echegaray, I. Arrechea-Marcos, A. Harillo-Baños, A. de la Peña, M. M. Ramos, J. T. López Navarrete, M. Campoy-Quiles, R. Ponce Ortiz and J. L. Segura, *J. Mater. Chem. C*, 2020, DOI: 10.1039/D0TC03026K.

3. P. García-Arroyo, M. P. Arrieta, D. Garcia-Garcia, R. Cuervo-Rodríguez, V. Fombuena, M. J. Mancheño and J. L. Segura, *Polymer*, 2020, **196**, 122466.

4. M. J. Frisch, et al., 2016, Gaussian 16, Revision C.01, Gaussian, Inc., Wallin.

5. S. Royuela, E. Martínez-Periñán, M. P. Arrieta, J. I. Martínez, M. M. Ramos, F. Zamora, E. Lorenzo and J. L. Segura, Chem. Commun., 2020, 56, 1267–1270.

6. P. Albacete, J. I. Martínez, X. Li, A. López-Moreno, S. Mena-Hernando, A. E. Platero-Prats, C. Montoro, K. P. Loh, E. M. Pérez and F. Zamora, J. Am. Chem. Soc., 2018, 140, 12922–12929.

7. S. Gámez-Valenzuela, M. Echeverri, B. Gómez-Lor, José I. Martínez and M. Carmen Ruiz-Delgado, 2020, DOI: 10.1039/D0TC03139A.

8.   J. P. Perdew, M. Ernzerhof and K. Burke, J. Chem. Phys., 1996, 105, 9982–9985.
9.   T. Yanai, D. P. Tew and N. C. Handy, Chem. Phys. Lett., 2004, 393, 51–57.
10.   W. J. Hehre, K. Ditchfield and J. A. Pople, J. Chem. Phys., 1972, 56, 2257–2261.
11.   M. M. Francl, W. J. Pietro, W. J. Hehre, J. S. Binkley, M. S. Gordon, D. J. DeFrees and J. A. Pople, J. Chem. Phys., 1982, 77, 3654–3665.
12.   T. H. Dunning, J. Chem. Phys., 1989, 90, 1007–1023.
13.   P. Giannozzi, et al., , J. Phys. Condens. Matter, 2009, 21, 395502.
14.   J. P. Perdew, K. Burke and M. Ernzerhof, Phys. Rev. Lett., 1996, 77, 3865–3868.
15.   S. Grimme, J. Comput. Chem., 2006, 27, 1787–1799.
16.   A. M. Rappe, K. M. Rabe, E. Kaxiras and J. D. Joannopoulos, Phys. Rev. B, 1990, 41, 1227–1230.
17.   N. Mounet and N. Marzari, Phys. Rev. B - Condens. Matter Mater. Phys., 2005, 71, 205214.
18.   J. D. Pack and H. J. Monkhorst, Phys. Rev. B, 1977, 16, 1748–1749.
19.   W. Humphrey, A. Dalke and K. Schulten, J. Mol. Graph., 1996, 14, 33–38.
20.   X. Ge, S. J. Binnie, D. Rocca, R. Gebauer and S. Baroni, Comput. Phys. Commun., 2014, 185, 2080–2089.
21.   O. B. Malcioğlu, R. Gebauer, D. Rocca and S. Baroni, Comput. Phys. Commun., 2011, 182, 1744–1754.